Journal of Materials Research and Technology 41 (2026) 4056–4066

Contents lists available at ScienceDirect

Journal of Materials Research and Technology

journal homepage: www.elsevier.com/locate/jmrt

Plasma nitriding of additively manufactured 316L austenitic stainless steel produced by laser power bed fusion and metal binder jetting

Nelson Filipe Lopes Dias [a,*], Julia Urbanczyk [a], Dominic Stangier [a,b], Patrick Köhnen [c], Christopher Schaak [c,1], Simon Höges [c], Wolfgang Tillmann [a]

[a] Institute of Materials Engineering, TU Dortmund University, Leonhard-Euler-Straße 2, 44227, Dortmund, Germany
[b] Oerlikon Balzers Coating Germany GmbH, Am Böttcherberg 30-38, 51427, Bergisch Gladbach, Germany
[c] GKN Powder Metallurgy GmbH & Co. KG, Pennefeldsweg 11-15, 53177, Bonn, Germany

ARTICLE INFO

Keywords:
Plasma nitriding
Laser power bed fusion
Metal binder jetting
Austenitic stainless steel
Microstructure
Hardness
Tribology

ABSTRACT

Among the additive manufacturing methods, laser powder bed fusion (L-PBF) and metal binder jetting (MBJ) are well established technologies for producing complex-shaped 316L components. Plasma nitriding provides an effective approach to enhance their surface properties, thereby broadening their application potential. Since L-PBF and MBJ generate distinct microstructures, it is essential to evaluate their influence on the resulting mechanical and tribological performance. Therefore, L-PBF- and MBJ-316L are plasma nitrided at temperatures of $T_{PN1} = 380$ °C and $T_{PN2} = 430$ °C for 10 h and compared with conventionally wrought 316L.

The thickness of the S phase is independent of the initial microstructure, exhibiting values of $\delta_{PN1} \approx 3$ µm at T_{PN1} and $\delta_{PN2} \approx 12$ µm at T_{PN2}. Nanoindentation reveals a significant increase in near-surface hardness to 1230–1400 HV_{IT} at T_{PN1} and 1420–1520 HV_{IT} at T_{PN2}, associated with austenite lattice expansion caused by interstitial dissolution of nitrogen. In contrast, Vickers microhardness is additionally influenced by the core microstructure, with plasma nitrided MBJ-316L showing lower values than L-PBF-316L. The enhanced surface hardness significantly improves the resistance against abrasive wear of all 316L variants. Overall, the plasma nitriding processes developed for conventionally manufactured 316L steels can be successfully applied to additively manufactured 316L.

1. Introduction

Additive manufacturing (AM) enables the production of complex-shaped geometries and customized steel parts with relatively short processing times, which are not achievable by conventional subtractive methods [1]. Laser powder bed fusion (L-PBF) and metal binder jetting (MBJ) are well-established powder-based AM methods for printing steel parts and components [2]. L-PBF employs a high power density laser beam to selectively melt and fuse steel powder in an inert gas atmosphere [3]. The molten pool rapidly solidifies to a thin layer, resulting in the layer-by-layer processing of the final part's 3D geometry. L-PBF-printed steels exhibit high density and refined microstructure with directional dendritic columns, leading to improved mechanical properties, such as high strength, ductility, and toughness [4]. Based on a different principle, the two-step MBJ process involves spreading a binding agent on the powder bed to layer-wise print a green body, which is then sintered in a high-temperature furnace [5]. Compared to L-PBF, MBJ allows for large-scale production of printed steel parts and components at higher build rates and lower production costs [6].

Among various steel grades, the austenitic chromium-nickel-molybdenum stainless steel AISI 316L (X2CrNiMo17-12-2) is widely used for commercial applications of L-PBF [7] and MBJ [8]. This low carbon-containing 316L steel demonstrates excellent corrosion resistance due to its alloying elements, making it suitable for diverse applications such as medical implants and instruments, maritime components as well as general engineering parts [9]. However, its low hardness and wear resistance impose restrictions on its usage in applications involving highly loaded mechanical contacts.

To overcome these limitations, the low temperature plasma nitriding of 316L offers an effective approach to enhance its subsurface near region, thereby expanding its fields of applications [10,11]. Nitriding at temperatures below $T < 450$ °C results in the formation of

* Corresponding author.
E-mail address: filipe.dias@tu-dortmund.de (N.F. Lopes Dias).
[1] Present Address: BleiStahl Services GmbH, Osterfelderstraße 51, 58300 Wetter.

https://doi.org/10.1016/j.jmrt.2026.02.042
Received 22 December 2025; Received in revised form 30 January 2026; Accepted 4 February 2026
Available online 5 February 2026

Table 1
Chemical composition of the differently manufactured 316L

Steel type	Chemical composition in wt.-%										
	Fe	Cr	Ni	Mn	Mo	Si	P	C	S	O	N
conv. 316L	68.42	17.52	9.81	1.55	2.25	0.27	0.03	0.02	0.03	0.01	0.09
L-PBF 316L	67.86	17.50	10.51	1.14	2.26	0.69	0	0.03	0.003	0	0.001
MBJ 316L	67.10	17.30	10.92	1.24	2.42	0.87	0.03	0.01	0.005	0.03	0.08

nitrogen-supersaturated austenite, with nitrogen atoms occupying octahedral interstitial sites. This phase is commonly referred to as expanded austenite γ_N or simply the S phase [12,13]. As a consequence, plasma nitrided 316L steel exhibits increased hardness and improved resistance against wear and corrosion [11,14,15]. At elevated nitrogen activity, however, the solubility limit of interstitial nitrogen in the austenitic matrix can be exceeded, promoting the formation of iron nitride phases, such as ε-Fe_3N and γ′-Fe_4N [16,17]. Moreover, nitriding temperatures above $T > 450$ °C results in the precipitation of chromium nitrides (CrN) [18,19]. The formation of CrN causes local chromium depletion in the austenitic matrix, which detrimentally affects the corrosion resistance of plasma nitrided 316L [12]. Consequently, controlled plasma nitriding at temperatures below $T < 450$ °C and at low nitrogen partial pressures leads to reduced nitrogen activity, thereby enabling the formation of expanded austenite, while suppressing the development of iron nitride compound layers and CrN precipitation [16].

Therefore, low temperature plasma nitriding presents a promising approach to enhance the surface properties of L-PBF and MBJ printed 316L steel, although it has received limited attention in the context of additively manufacturing. In an initial study, Godec et al. demonstrated that plasma nitriding improves the wear and corrosion resistance of L-PBF processed 316L with comparable properties to plasma nitrided wrought 316L [20]. Lin et al. compared nitrided layers on L-PBF-316L and wrought 316L after plasma nitriding at 440 °C for 15 h [21]. They found that L-PBF-316L, despite having a comparable density to its wrought counterpart, developed a thicker nitrided layer. This was attributed to enhanced nitrogen diffusion driven by several factors associated with the heterogeneous L-PBF-316L microstructure: increased atomic spacing due to tensile stresses, dislocation networks within subgrains, higher grain boundary density, and similar crystallographic orientations in columnar grains. Kumar et al. studied the influence of build orientation (0°, 45°, and 90° to the surface) on the plasma nitriding behavior of L-PBF-316L [22]. After nitriding at 500 °C for 10 h, they observed a decrease in nitrided layer thickness in the order $0° > 45° > 90°$, which they attributed to incomplete pre-etching of the native oxide layer. The passivation layer was found to be thicker in L-PBF-316L with finer grain sizes, following the order $90° > 45° > 0°$. In contrast, Yazıcı et al. plasma nitrided L-PBF-316L with identical build orientations at 400 °C for 4 h and reported an opposite trend in nitrided layer thickness, decreasing in the order of 90°, 45°, and 0° (note that, in their study, 90° corresponds to a horizontally oriented surface and 0° to a vertically oriented one; angle values have been adjusted here for consistency to the study by Kumar et al.) [23]. The thicker nitrided layer observed at the 90° orientation was attributed to smaller melt pool sizes, which were considered to enhance nitrogen diffusion.

These studies underscore the complexity of plasma nitriding of additively manufactured 316L, where factors such as initial microstructure and pre-treatment significantly influence nitrogen diffusion. However, a systematic understanding of how different additive manufacturing routes influence the S phase formation is still lacking. In particular, the plasma nitriding behavior of MBJ-316L remains largely unexplored. To gain a comprehensive insight into the effect of microstructural characteristics induced by additive manufacturing on the properties of the plasma nitrided layer, steel variants were fabricated through conventional hot-rolling, L-PBF, and MBJ methods. Subsequently, the 316L steel variants were plasma nitrided at temperatures of $T_{PN1} = 380$ °C and $T_{PN2} = 430$ °C for $t = 10$ h. These temperatures were selected to promote the formation of expanded austenite while suppressing the precipitation of CrN. The two temperature levels further enable a comparison of different nitrogen diffusion regimes, which is reflected in variations in the thickness of the nitrided layers. Finally, the structural, mechanical, and tribological properties were systematically characterized in both the non-treated and plasma nitrided conditions.

2. Experimental details

316L discs were produced with a cylindrical geometry with a diameter of $\phi = 40$ mm and a height of $h = 5$ mm. The MBJ processing of 316L is explained in more detail in Ref. [24]. The chemical composition of the conventionally and additively manufactured steel is given in Table 1. The densities were determined to be $\rho = 7.99$ g/cm^3 for conventionally manufactured 316L, $\rho = 7.95$ g/cm^3 for L-PBF printed 316L, and $\rho = 7.69$ g/cm^3 for MBJ printed 316L. Prior to the plasma nitriding process, the 316L parts were ground and mirror-polished by metallographic preparation.

The plasma nitriding process was carried out using an industrial physical vapor deposition device METAPLAS.DOMINO kila flex (Oerlikon Balzers Coating Germany GmbH, Germany). The entire procedure, including evacuating and heating, prior ion etching and subsequent plasma nitriding, was conducted with enhanced plasma excitation through the advanced arc-enhanced glow discharge (AEGD) technology, ensuring a highly plasma excitation. The detailed functionality of AEGD is described elsewhere [25]. Compared to conventional glow discharges, AEGD not only ensures higher etch rates but also enables plasma nitriding with controlled hardness gradients. Following chamber evacuation and heating to the intended plasma nitriding temperature, the 316L steel variants underwent ion etching for 60 min using highly ionized argon ions in the AEGD mode. The specific ion etching parameters are described in detail in Ref. [26]. The etching procedure removes native oxides from the surface, promoting thereby the diffusion of nitrogen into 316L [27]. The 316L steel variants were plasma nitrided under AEGD in an argon-nitrogen-hydrogen atmosphere with a nitrogen-to-hydrogen ratio of 1:2 at a constant pressure of $p = 1.5 \times 10^{-2}$ mbar ($p = 1500$ mPa) for $t = 10$ h. The heating power was adjusted to obtain a substrate temperature of approximately $T_{PN1} = 380$ °C and $T_{PN2} = 430$ °C. A pulsed bias voltage of $U_b = -150$ V with a mid-frequency of $f = 20$ kHz and a duty cycle of 80 % was applied to the substrates.

The non-treated and plasma nitrided 316L substrates underwent metallographic preparation and etching with Marble's reagent for subsequent evaluation of the nitrided layer's morphology and thickness using white light microscopy. Scanning electron microscopy (SEM) analysis additionally assessed the surface topography of the 316L substrates at each processing step.

Furthermore, a confocal 3D microscope μsurf (NanoFocus GmbH, Germany) was employed to quantify the average mean roughness *Ra* and mean roughness depth *Rz*. In accordance with DIN EN ISO 21920-3:2022-12 [28], the measurement areas were adjusted based on the required sampling and evaluation lengths for each surface state. Data analysis was performed using MountainsMap 8 (DigitalSurf, France). To ensure high statistical accuracy, all available profiles within the measured areas were extracted and averaged. Three distinct measurements were performed for each 316L steel variant to calculate mean

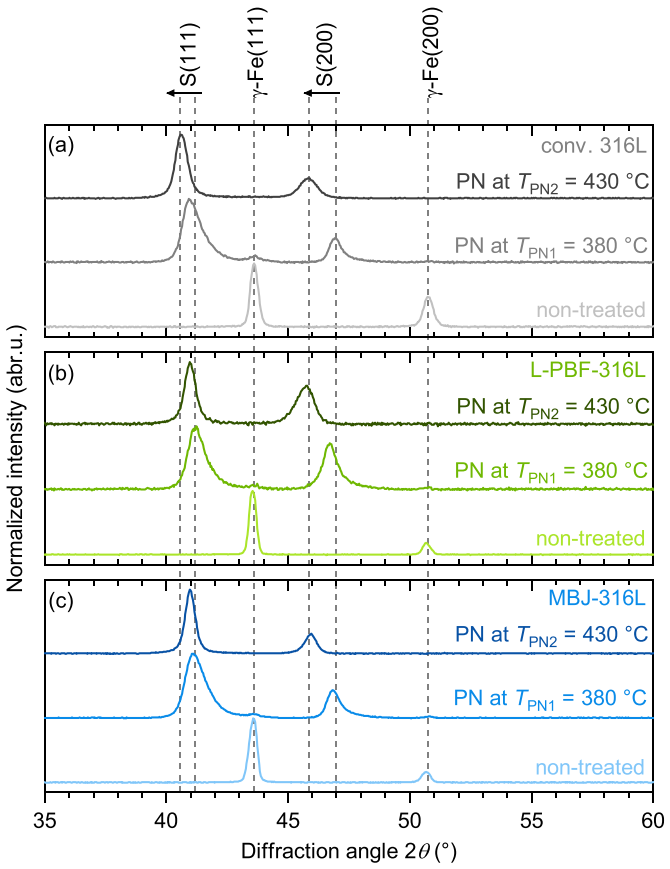

Fig. 1. X-ray diffractograms of (a) conventionally manufactured, (b) L-PBF printed, and (c) MBJ printed 316L in non-treated and plasma nitrided conditions. For clarity, the diffractograms are shown over a diffraction angle range 2θ from 35° to 60°. The complete diffractograms covering 2θ from 30° to 120° are provided in Fig. A of the Supplementary Materials.

values and standard deviations.

X-ray diffraction (XRD) analyses were carried out using a D8 Advance (Bruker AXS GmbH, Germany) equipped with a polycapillary parallel x-ray lens of 2 mm and a LynxEye silicon strip detector (Bruker AXS GmbH, Germany). The x-rays were generated using Cu-Kα radiation ($\lambda = 0.15418$ nm) source at a voltage of 40 kV and a current of 40 mA. The x-ray diffractograms were obtained in Bragg-Brentano geometry over a scanning range from 30° to 120° with a scan step of $\Delta 2\theta = 0.035°$ and an exposure time of $t = 1$ s per scan step. For CrNi-based austenitic steels, the corresponding penetration depth within the γ-Fe phase extends from approximately $z_0 = 0.9$ μm for the (111) angle at $2\theta = 43.6°$ to $z_0 = 2.0$ μm for the (400) angle at $2\theta = 118.2°$ [29].

Vickers microhardness tests using a load of 20 g were performed to determine the microscopic hardness, with 6 indentations per non-treated and plasma nitrided 316L steel variant. In addition, nanoindentation was performed using a NHT3 nanoindenter (Anton Paar GmbH, Austria) equipped with a Berkovich diamond tip to more accurately assess the near-surface hardness of the nitrided layer while minimizing the influence of the core material. The measurements were performed under load-control mode with a maximum load of $F = 15$ mN, comprising 40 indentations for each steel type in the respective condition.

The tribological properties were analyzed using a ball-on-disc tribometer THT (Anton Paar Group AG, Austria). An AISI 52100 (100Cr6) steel ball with a diameter of $\varnothing = 6$ mm and a hardness of (1150 ± 20) HV 0.02 was used as the counterpart. The tests were conducted with a normal load of $F_N = 2$ N, a relative velocity of $v = 0.4$ m/s, and a total of 2000 rotations in ambient air at room temperature under dry sliding condition. The wear rate of the 316L steels was calculated through the determination of the wear volumes with an optical 3D surface analyzer Infinite Focus (Alicona Imaging GmbH, Austria). In addition, the wear tracks of the non-treated and plasma nitrided 316L steels were investigated by SEM to identify the wear mechanisms. Furthermore, the wear rate of the AISI 52100 counterpart was calculated using the geometric formula for the volume of a ball segment, based on light micrographs.

3. Results and discussion

3.1. Crystallographic structure

The crystalline phases present in the non-treated and plasma nitrided 316L substrates were analyzed by XRD. Fig. 1 presents the x-ray diffractograms in the 2θ range from 35° to 60° to provide a focused overview of the most relevant crystallographic changes, while the complete diffractograms measured over the full scanning range from 30° to 120° are provided in Fig. A of the Supplementary Material. For all non-treated 316L variants, the diffractograms exhibit Bragg reflections of the γ-Fe phase, with a pronounced preferred orientation along the (111) plane. The calculated lattice parameters a_{hkl}, derived from the corresponding interplanar spacings d_{hkl}, are summarized in Table 2. The Nelson-Riley extrapolation method allows for the precise determination of the lattice parameter a_0 of the face-centered cubic γ-Fe phase. In this approach, the individual a_{hkl} values are plotted as a function of the Nelson-Riley function, and a linear fit is extrapolated to $f(\theta) = 0$, corresponding to a diffraction angle of $2\theta = 180°$, where systematic instrumental errors are minimized [30]. The corresponding Nelson-Riley plots for the different steel variants are shown in Fig. B of the Supplementary Material. Using this method, the lattice parameters of $a_0 = 3.598$ Å for conventionally manufactured 316L, $a_0 = 3.595$ Å for L-PBF-316L, and $a_0 = 3.596$ Å for MBJ-316L were obtained. These results indicate that, despite the different manufacturing routes, all 316L substrates exhibit comparable γ-Fe lattice parameters, which is consistent with their similar chemical compositions.

For the plasma nitrided 316L steel variants, the diffractograms show broadening and a shift of the Bragg reflections towards lower diffraction

Table 2
Individual lattice parameters a_{hkl} obtained from the (111), (200), (220), (311), (222), and (400) Bragg angles as well as lattice parameters a_0 determined using the Nelson-Riley method for conventionally manufactured, L-PBF printed, and MBJ printed 316L in non-treated and plasma nitrided conditions.

manufacturing method	treatment condition	a_{111} in Å	a_{200} in Å	a_{220} in Å	a_{311} in Å	a_{222} in Å	a_{400} in Å	a_0 in Å
conv. 316L	non-treated	3.592	3.594	3.594	3.597	3.596	3.597	3.598
	PN at T_{PN1} = 380 °C	3.815	3.869	-	3.849	3.829	-	3.844
	PN at T_{PN2} = 430 °C	3.848	3.958	3.899	3.900	3.845	-	3.874
L-PBF-316L	non-treated	3.597	3.599	3.596	3.595	3.595	3.597	3.595
	PN at T_{PN1} = 380 °C	3.792	3.886	-	3.845	-	-	3.868
	PN at T_{PN2} = 430 °C	3.812	3.964	-	3.909	-	-	3.949
MBJ-316L	non-treated	3.595	3.600	3.596	3.598	3.595	3.595	3.596
	PN at T_{PN1} = 380 °C	3.802	3.875	-	3.835	3.875	-	3.867
	PN at T_{PN2} = 430 °C	3.812	3.949	-	3.905	3.822	-	3.870

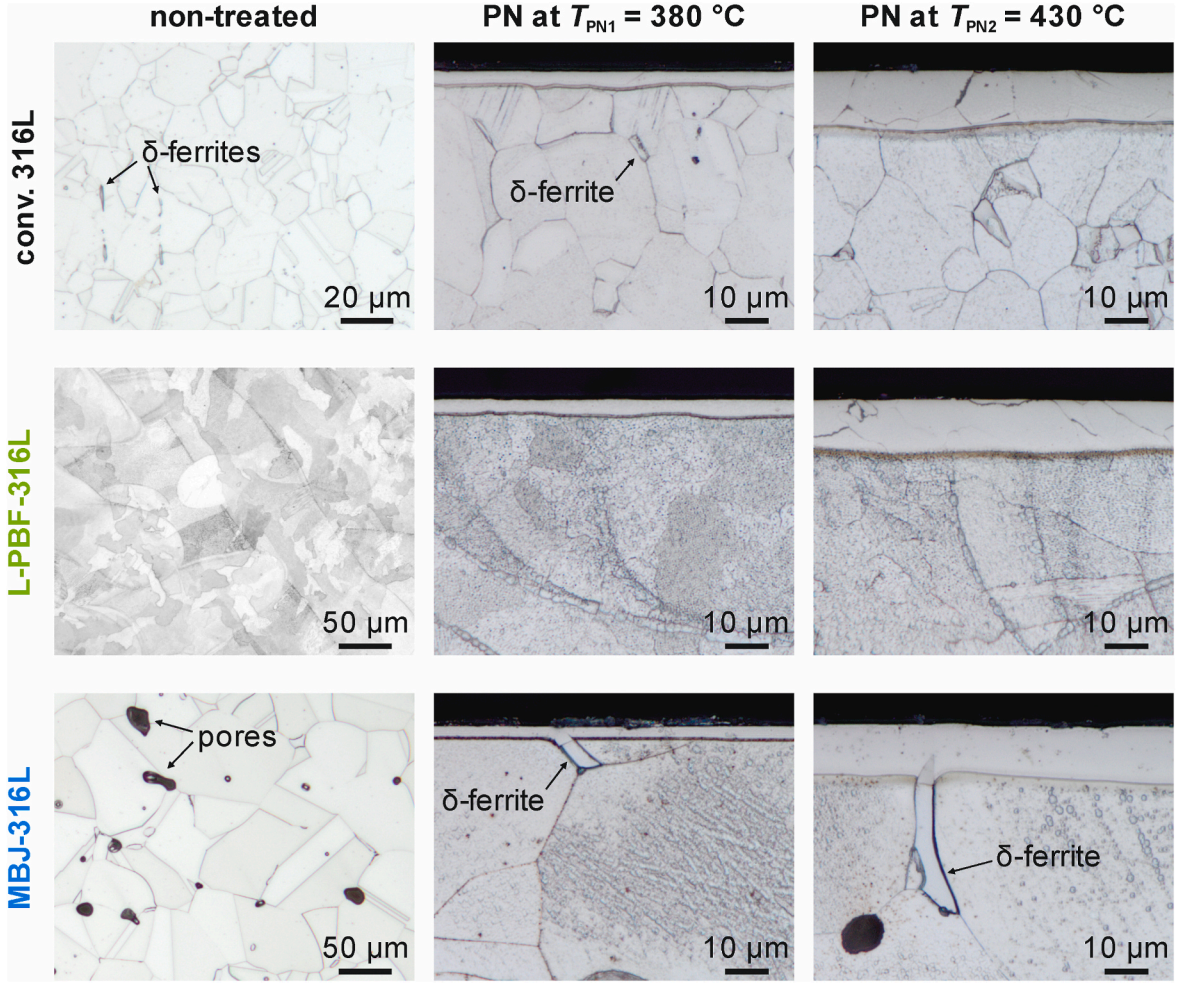

Fig. 2. Light optical micrographs of the conventionally manufactured (conv.) 316L, L-PBF 316L, and MBJ 316L in non-treated and plasma nitrided conditions.

angles. These changes stem from the expansion of the γ-Fe lattice due to the interstitial dissolution of nitrogen [31]. Notably, at the highest plasma nitriding temperature T_{PN2}, an additional shift towards lower diffraction angles is observed, indicating a higher degree of lattice expansion for the S phase. In addition, the angular distance between the (111) and (200) reflections is reduced in the plasma nitrided steels compared to the non-treated condition. This reduction is more pronounced for the steel variants plasma nitrided at T_{PN2} than for those treated at the lower temperature T_{PN1}. No diffraction angles corresponding to ε-Fe_3N, γ′-Fe_4N, or CrN were detected, confirming that the applied plasma nitriding conditions effectively suppressed their formation. This is attributed to the combination of nitriding temperatures maintained below $T < 450$ °C and reduced nitrogen partial pressures, which favor the stabilization of expanded austenite while preventing nitride precipitation.

Notably, the Bragg angles of the S phase exhibit a pronounced asymmetry toward higher angle values for the 316L steel variants plasma nitrided at T_{PN1} compared to those treated at T_{PN2}. Considering that the maximum x-ray penetration depth is approximately 2 µm, the diffracting volume in the steel variants plasma nitrided at T_{PN1} encompasses almost the entire thickness of the nitrided layer. In contrast, the substantially thicker nitrided layers formed at T_{PN2} extend well beyond the x-ray penetration depth, as confirmed by the light optical micrographs presented in the subsequent section. As a result, the nitrogen concentration gradient within the thinner nitrided layer exerts a stronger influence on the diffraction signal, potentially resulting in peak asymmetry. For the thicker nitrided layers, the diffraction response is dominated by the near-surface region with a more homogeneous nitrogen content, resulting in less pronounced peak asymmetry.

It is observed that, for some plasma nitrided 316L steel variants, the Bragg reflections corresponding to the (220), (222), and (400) planes are no longer detectable, as shown in Fig. A of the Supplementary Material. The lattice parameters a_{hkl} calculated from the respective diffraction planes of the plasma nitrided 316L steels as well as the values a_0 determined from the Nelson-Riley extrapolation are summarized in Table 2. Plasma nitriding induces a pronounced expansion of the γ-Fe lattice. As expected, the higher plasma nitriding temperature T_{PN2} results in a greater lattice expansion compared to T_{PN1}. Notably, the lattice expansion associated with the (200) plane is more pronounced than that of the other crystallographic planes. Across the different 316L steel variants, plasma nitriding at T_{PN2} leads to lattice expansions of approximately 6-7% for the (111) plane and up to approximately 10% for the (200) plane. This anisotropic lattice expansion is further reflected in the Nelson-Riley extrapolation plots shown in Fig. B of the Supplementary Material, where the individual a_{hkl} values deviate significantly from the linear regression expected for an ideal face-centered cubic lattice, resulting in substantial scatter about the extrapolation line. Consequently, the lattice parameters a_0 determined by the Nelson-Riley method may not reliably represent the true lattice parameter under conditions of pronounced anisotropic lattice expansion.

Such anisotropic expansion is commonly reported for the S phase of plasma nitrided 316L. Different hypotheses have been proposed to explain this phenomenon, as concisely reviewed by Borgioli et al. [32]. Several studies suggest that the presence of phases with different lattice

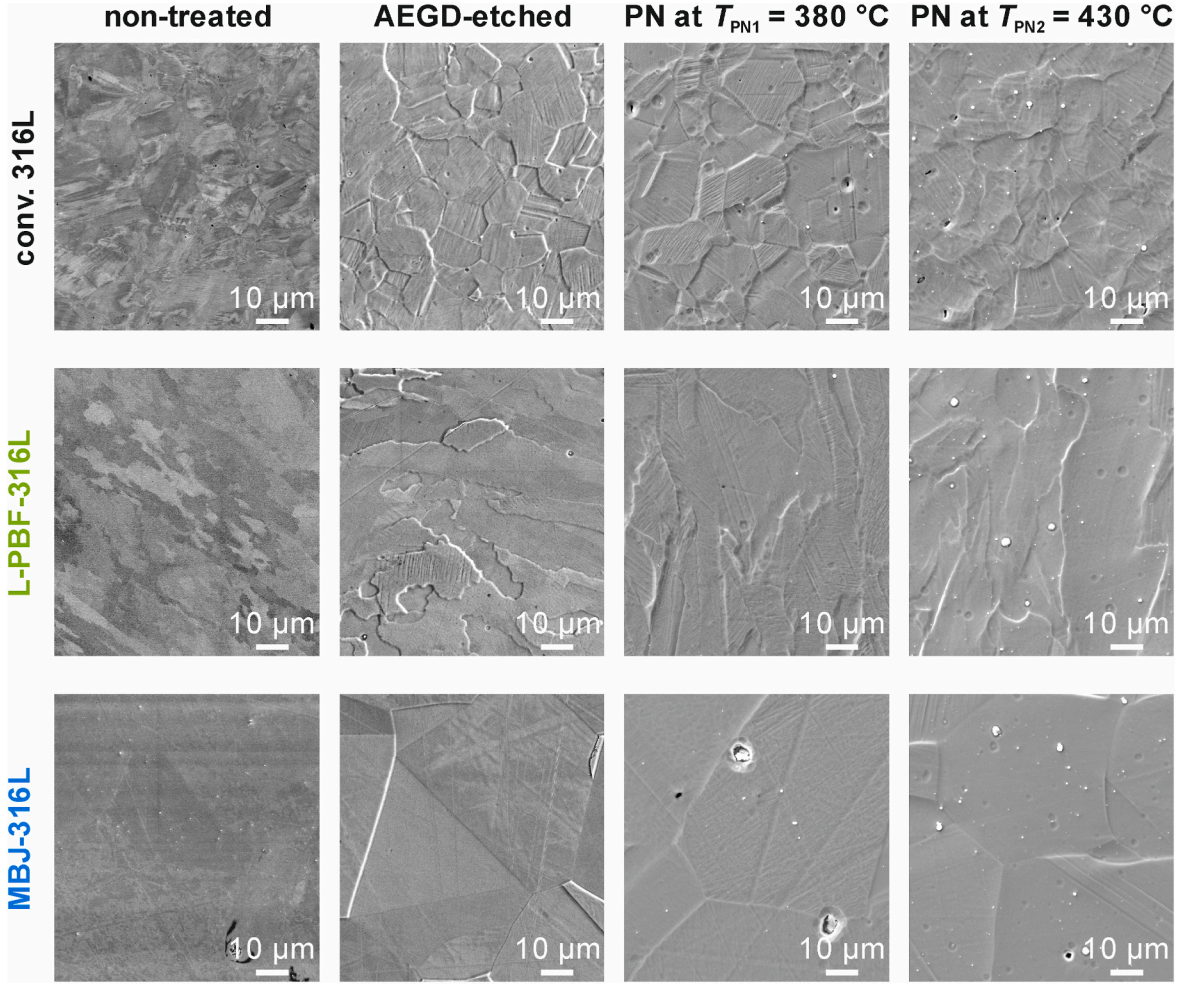

Fig. 3. SEM micrographs of the topography of conventionally manufactured (conv.) 316L, L-PBF-316L, and MBJ-316L in non-treated and polished, AEGD etched, and plasma nitrided condition.

parameters [33,34] or distortions of the austenite lattice may result in a face-centered tetragonal [35,36] or body-centered tetragonal structure [37]. Additionally, the occurrence of stacking faults has been identified as a possible mechanism for the anisotropic expansion [38]. For a comprehensive discussion of these hypotheses, reference is made to the work of Borgioli et al. [32].

3.2. Microstructure

The microstructure of the non-treated and plasma nitrided 316L substrates was investigated using light optical microscopy analyses (see Fig. 2). Conventional manufacturing of 316L steel reveals a microstructure consisting of austenitic grains with a small amount of δ-ferrites. The retention of residual δ-ferrite after solidification is a common observed effect in austenitic stainless steels [39]. The sintering process in MBJ leads to the formation of larger austenitic grains, with a minor presence of the δ-ferrite phase also observed in the microstructure. Additionally, MBJ-316L exhibits residual porosity, leading to a lower density compared to the other manufacturing methods. In contrast, L-PBF-316L displays distinct solidified melt pools with a parabolic shape and sharp melt pool boundaries, along with an absence of residual pores. Furthermore, the microstructure of L-PBF-316L steel reveals small δ-ferrite grains along the melt pool boundaries. For all 316L variants, the XRD analyses did not detect the presence of the δ-ferrite phase, indicating that both conventionally manufactured 316L, L-PBF-316L, and MBJ-316L have very low amounts of residual δ-ferrite.

The plasma nitriding forms an expanded austenite on the surface of the differently manufactured 316L, whose thickness is governed solely by the nitriding temperature. Regardless of the manufacturing method, the thickness of the S phase layer in the nitrided 316L steel is approximately $\delta_{PN1} \approx 3$ µm when plasma nitrided at $T_{PN1} = 380$ °C, while a higher nitriding temperature of $T_{PN2} = 430$ °C promotes a larger thickness of around $\delta_{PN1} \approx 12$ µm. Therefore, the microstructure of the differently manufactured 316L steels does not significantly impact the nitriding depth. This finding aligns well with a previous study by Godec et al. [20], who reported similar thicknesses of the nitrided S phase layer for conventionally manufactured, L-PBF printed and additionally solution-treated 316L under identical nitriding conditions. This supports the understanding that the formation of this expanded phase involves thermally activated interstitial diffusion of nitrogen atoms in austenite [40]. Given that the γ-Fe lattice of the differently manufactured 316L steels possesses almost identical lattice parameters, it can be expected that the diffusion rates are comparable, resulting in similar nitriding depths. Interestingly, for MBJ-316L, it is also noted that the nitrided layer appears deeper within δ-ferrite grains compared to austenite, likely due to the higher diffusion rates in body-centered cubic ferrite than in face-centered cubic austenite [32].

However, the comparable thicknesses of the nitrided S phase observed for the differently manufactured 316L substrates stand in contrast to the findings of Lin et al., who reported variations between L-PBF-316L and wrought 316L [21], as well as to those of Kumar et al. and Yazıcı et al., who observed different thicknesses for L-PBF-316L

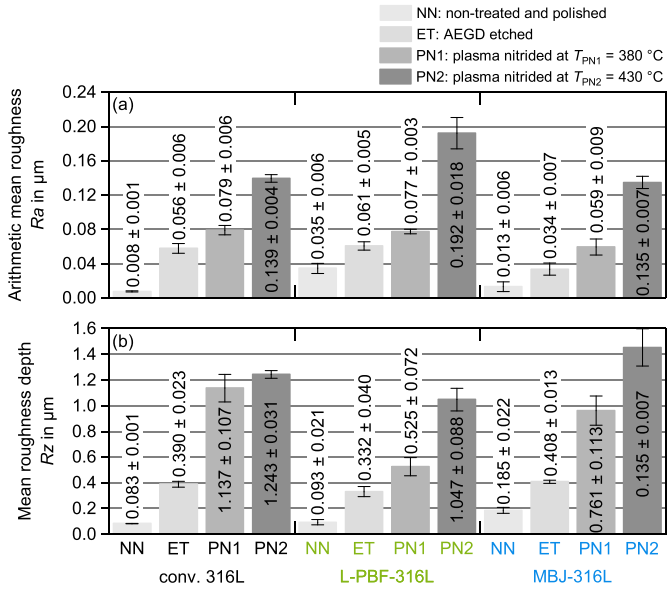

Fig. 4. (a) Arithmetic mean roughness *Ra* and (b) mean roughness depth *Rz* of conventionally manufactured (conv.) 316L, L-PBF-316L, and MBJ-316L in non-treated and polished, AEGD etched and plasma nitrided conditions.

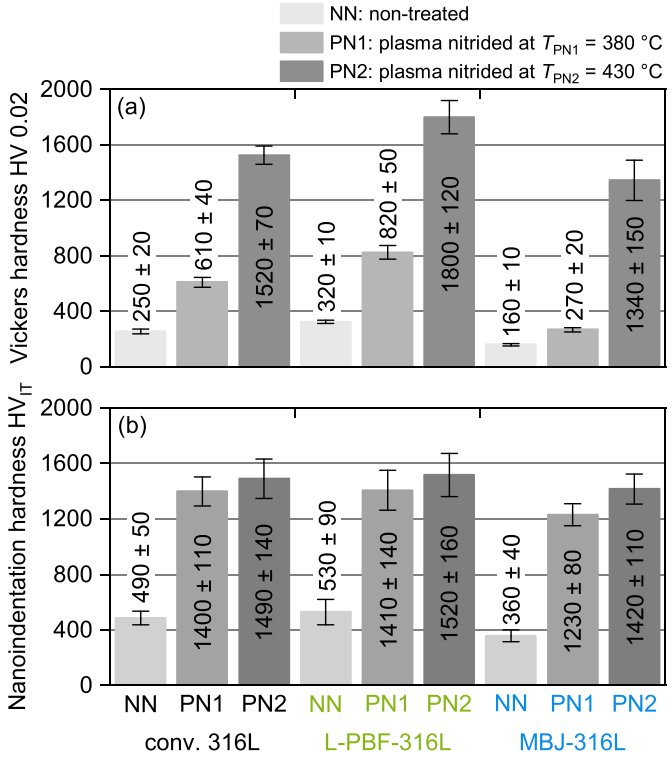

Fig. 5. (a) Vickers hardness HV 0.02 and (b) nanoindentation hardness of the conventionally manufactured(conv.) 316L, L-PBF-316L, and MBJ-316L in non-treated and plasma nitrided conditions.

fabricated with varying build orientations [22,23]. As suggested by Lin et al. [21], such discrepancies may be attributed to pronounced microstructural differences, particularly increased atomic spacing due to tensile stresses, dislocation networks within subgrains, and similar crystallographic orientations in columnar grains, whereas a higher grain boundary density can be excluded in the present case. In addition, an alternative explanation could be insufficient removal of the native oxide layer during the etching sequence, which, depending on the

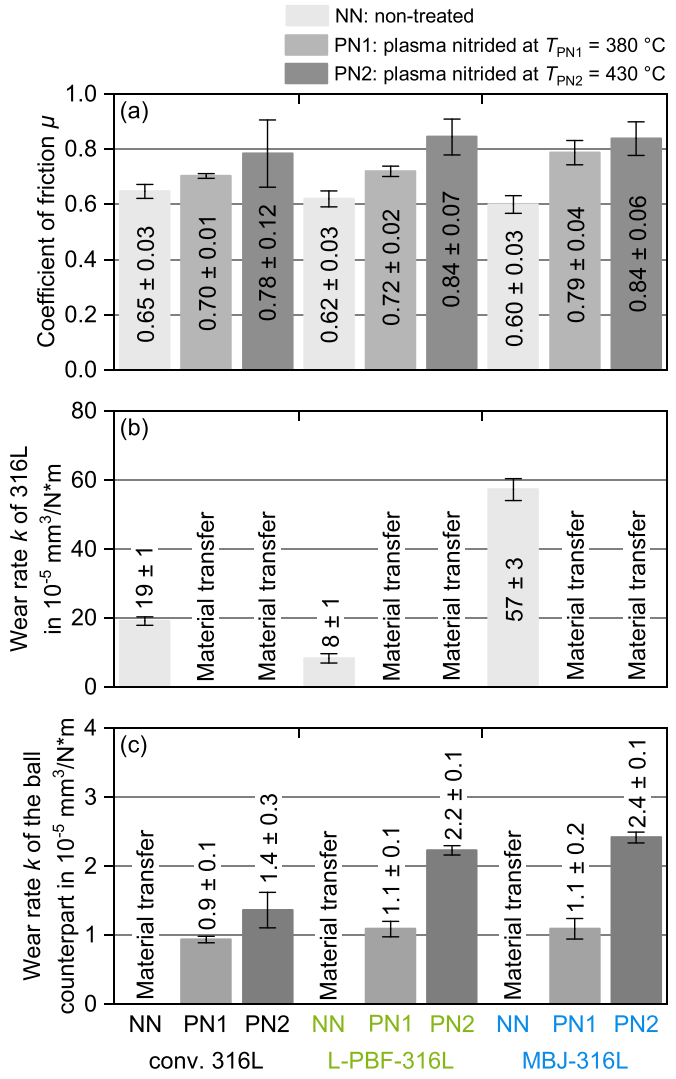

Fig. 6. (a) Coefficients of friction and (b) wear rates of the conventionally manufactured (conv.) 316L, L-PBF-316L, and MBJ-316L in non-treated and plasma nitrided conditions, along with (c) wear rates of the AISI 52100 ball counterparts, obtained from tribometer tests.

microstructure, may hinder nitrogen diffusion and thereby influence the thickness of the S phase.

3.3. Topography and roughness

SEM analyses were employed to investigate the topography of the 316L steels across the different processing step, as shown in Fig. 3. This included the polished initial state, AEGD-etched state, and the plasma nitrided condition. These observations aimed to assess the progressive alterations on the surfaces of the differently manufactured 316L steels throughout the entire process. The corresponding roughness values *Ra* and *Rz* for each state are presented in Fig. 4a and b, respectively. In non-treated condition, both L-PBF-316L and MBJ-316L exhibit higher surface roughness compared to conventionally manufactured 316L in the non-treated condition. These differences in roughness can be attributed to the variations in microstructure. The melt pool structure characteristic of L-PBF-316L and the presence of larger grains in MBJ-316L contribute to a rougher surface compared to conventionally manufactured 316L with its smaller grain size.

The surfaces of the etched steels exhibit significant material removal, a consequence of the notably high etch rate associated with the AEGD ion etching process. This process is characterized by an elevated degree

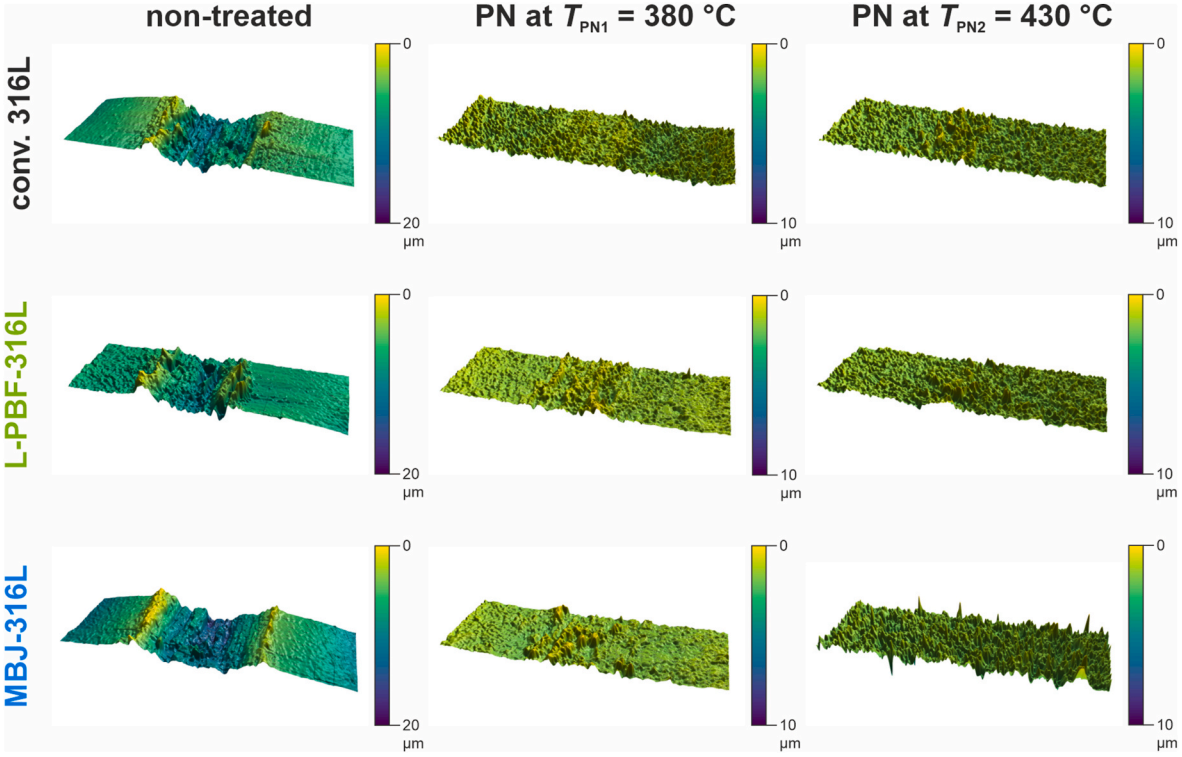

Fig. 7. 3D profiles of the wear track of the conventionally manufactured (conv.) 316L, L-PBF 316L, and MBJ 316L in non-treated and plasma nitrided conditions after the tribometer tests against AISI 52100 ball counterparts.

of argon ionization [41]. The etched surfaces reveal variations in etch depth across individual grains, making grain boundaries distinctly visible. In ion etching procedures, high-energy argon ion bombardment induces material sputtering. The sputtering rate depends not only on the kinetic energy of the impinging ions and the bonding energy of the material but also on the crystallographic orientation of the individual grains [42]. These differing orientations lead to the observed variations in etch depth. Consequently, the AEGD ion etching process increases the surface roughness for the differently manufactured 316L steels, deviating from the roughness trend observed in the initial, non-treated state.

In addition, the etched surfaces reveal the presence of slip bands within the grains. This is more prominent in the finer-grained conventionally manufactured 316L and L-PBF-316L. Previous studies focused primarily on plasma nitrided surfaces and suggested that slip bands form due to expansion-induced grain deformation [43–45]. However, the observations of slip bands in the etched, pre-nitrided state suggest a different origin. The etching process itself is unlikely to generate sufficient strain to induce slip beyond the yield point, given its atom-by-atom removal. Therefore, the formation of slip bands can likely be attributed to the metallographic preparation steps involving lapping and polishing. In particular, lapping can induce strain hardening in the steel. Due to the varying crystallographic orientations of different planes within the grains, the slip bands etched differently compared to the surrounding material, making them visible after etching.

Plasma nitriding induces grain-to-grain swelling with out-of-plane deformation, particularly at the highest nitriding temperature T_{PN2} = 430 °C. Dissolved nitrogen within the lattice expands the grain volume. However, neighboring grains hinder this expansion in parallel directions, leading to a pronounced effect perpendicular to the surface [31]. Consequently, grain swelling amplifies surface roughness. As expected, elevated nitriding temperatures lead to increased lattice expansion, reflected in a consistent rise in roughness values *Ra* and *Rz* for the plasma nitrided 316L steels. This trend is evident, with 316L steels plasma nitrided at T_{PN2} = 430 °C exhibiting the highest roughness values *Ra* and *Rz* among each respective manufacturing method. In conclusion, the observed increase in roughness is a combined effect of the AEGD ion etching and the plasma nitriding process. This highlights the importance of considering the effect of each processing step on the final surface characteristics.

3.4. Mechanical properties

The Vickers microhardness HV 0.02 of the non-treated and plasma nitrided 316L is shown in Fig. 5a, while the near-surface hardness determined by nanoindentation is presented in Fig. 5b. For comparability with the Vickers measurements, the nanoindentation hardness values are presented on the Vickers hardness scale HV. In the non-treated state, L-PBF-316L exhibits a higher Vickers hardness of (320 ± 10) HV 0.02 compared to conventionally manufactured 316L with (250 ± 10) HV 0.02. This elevated Vickers microhardness of L-PBF-316L is attributed to a combination of twin boundaries, dislocation networks, and grain refinement [46]. Contrarily, MBJ-316L has the lowest hardness of (160 ± 10) HV 0.02 due to its larger grain size and lower density [24,47]. In the near-surface region, a similar trend among the non-treated 316L steels is observed. However, higher hardness values are obtained with (490 ± 50) HV_{IT} for conventionally manufactured 316L, (530 ± 90) HV_{IT} for L-PBF-316L, and (360 ± 40) HV_{IT} for MBJ-316L. The increased near-surface hardness compared to the Vickers microscopic hardness values is attributed to strain hardening introduced during metallographic preparation, particularly by the grinding step, which induces plastic deformation in the surface region.

Plasma nitriding significantly increases the hardness of 316L produced with each manufacturing method. When considering the Vickers microhardness, significantly higher hardness values are achieved for the 316L steels plasma nitrided at the highest temperature T_{PN2} = 430 °C compared to those plasma nitrided at T_{PN1} = 380 °C. The trend in Vickers hardness values observed for the different manufacturing methods is maintained after plasma nitriding. At the highest plasma nitriding temperature of T_{PN2} = 430 °C, L-PBF-316L reaches the highest Vickers hardness of (1800 ± 120) HV 0.02, whereas MBJ-316L has the

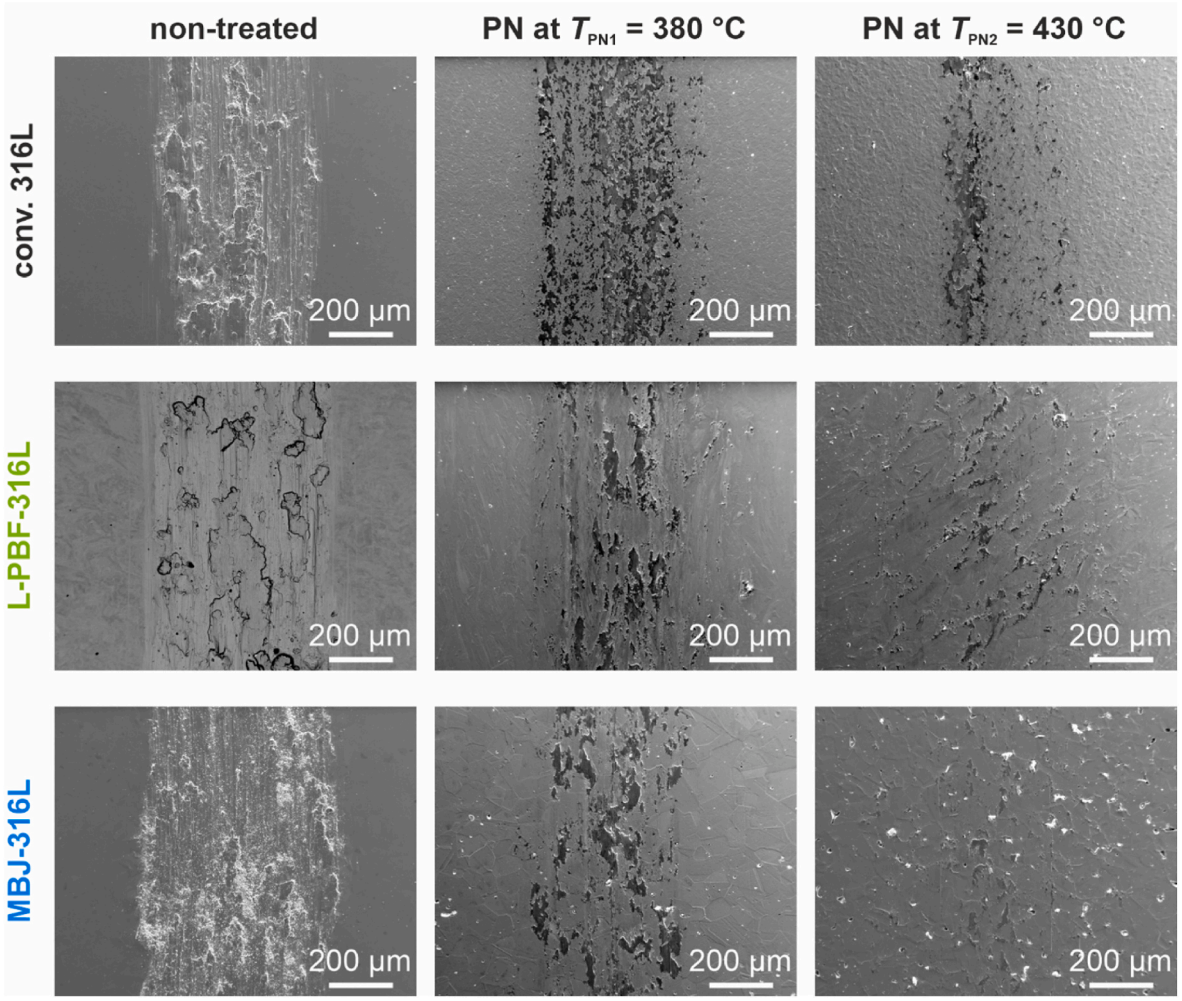

Fig. 8. SEM micrographs of the wear track of the conventionally manufactured (conv.) 316L, L-PBF 316L, and MBJ 316L in non-treated and plasma nitrided conditions after the tribometer tests against AISI 52100 steel counterparts.

lowest Vickers hardness of (1340 ± 140) HV 0.02. In contrast, all 316L variants plasma nitrided at $T_{PN2} = 380$ °C show lower Vickers hardness values. Since the Vickers measurement is significantly affected by the core hardness, a reduced thickness of the S phase layer results in lower Vickers microhardness values.

However, when considering the near-surface hardness, the differences between the plasma nitrided steels are considerably smaller compared to the Vickers hardness values. For example, L-PBF-316L plasma nitrided at $T_{PN2} = 430$ °C exhibits a hardness of (1520 ± 160) HV_{IT}, while a slightly reduced hardness of (1410 ± 140) HV_{IT} is obtained after plasma nitriding at $T_{PN1} = 380$ °C. Since nanoindentation primarily measures the near-surface region and thus predominantly captures the hardness of the S phase layer, the results indicate that even an S phase layer with a thickness of $\delta_{PN1} \approx 3$ µm achieves very high hardness values. The slightly higher hardness values observed at $T_{PN2} = 430$ °C are attributed to the greater lattice expansion of the S phase, as confirmed by XRD analyses. Among the different 316L manufacturing methods, the trend in hardness remains consistent, with L-PBF-316L, conventionally manufactured 316L, and MBJ-316L steels showing decreasing hardness, similar to the Vickers hardness measurements. Although nanoindentation focuses on the near-surface region, a minor influence of the core hardness is still present. Furthermore, a higher Vickers hardness of (1800 ± 120) HV 0.02 was measured for L-PBF-316L plasma nitrided at $T_{PN2} = 430$ °C compared to the value obtained by nanoindentation. This behavior can be attributed to the initial microstructure of the L-PBF-316L, where grain refinement and a high dislocation density contribute to an increased Vickers microhardness, which is more distinctly captured due to the thicker S phase layer.

Therefore, the increase in hardness of plasma nitrided 316L is primarily attributed to the expansion of the γ-Fe lattice caused by the interstitial dissolution of nitrogen. However, both the thickness of the S phase layer and the core hardness influence the Vickers microhardness of plasma nitrided 316L. These factors must be considered when plasma nitriding additively manufactured 316L with varying microstructures, especially since most studies report only Vickers hardness values.

3.5. Tribological properties

The tribological properties were evaluated in tribometer tests using AISI 52100 ball counterparts. Fig. 6 shows the coefficients of friction (COF) and wear rates of the non-treated and plasma nitrided 316L steels as well as the wear rates of the ball counterparts. The corresponding 3D profiles and SEM micrographs of the wear tracks are presented in Figs. 7 and 8, respectively, while light micrographs of the worn AISI 52100 ball counterparts are shown in Fig. 9.

Among the different conditions, the non-treated steels exhibit the lowest COF values ranging from $\mu \approx 0.6$ to $\mu \approx 0.65$. The additively manufactured steels tend to show slightly lower friction compared to conventionally manufactured 316L steel. However, when considering the standard deviation, the COF values remain almost at the same level. In contrast, the wear behavior is significantly influenced by the manufacturing method. L-PBF-316L exhibits the lowest wear rate of $k \approx$

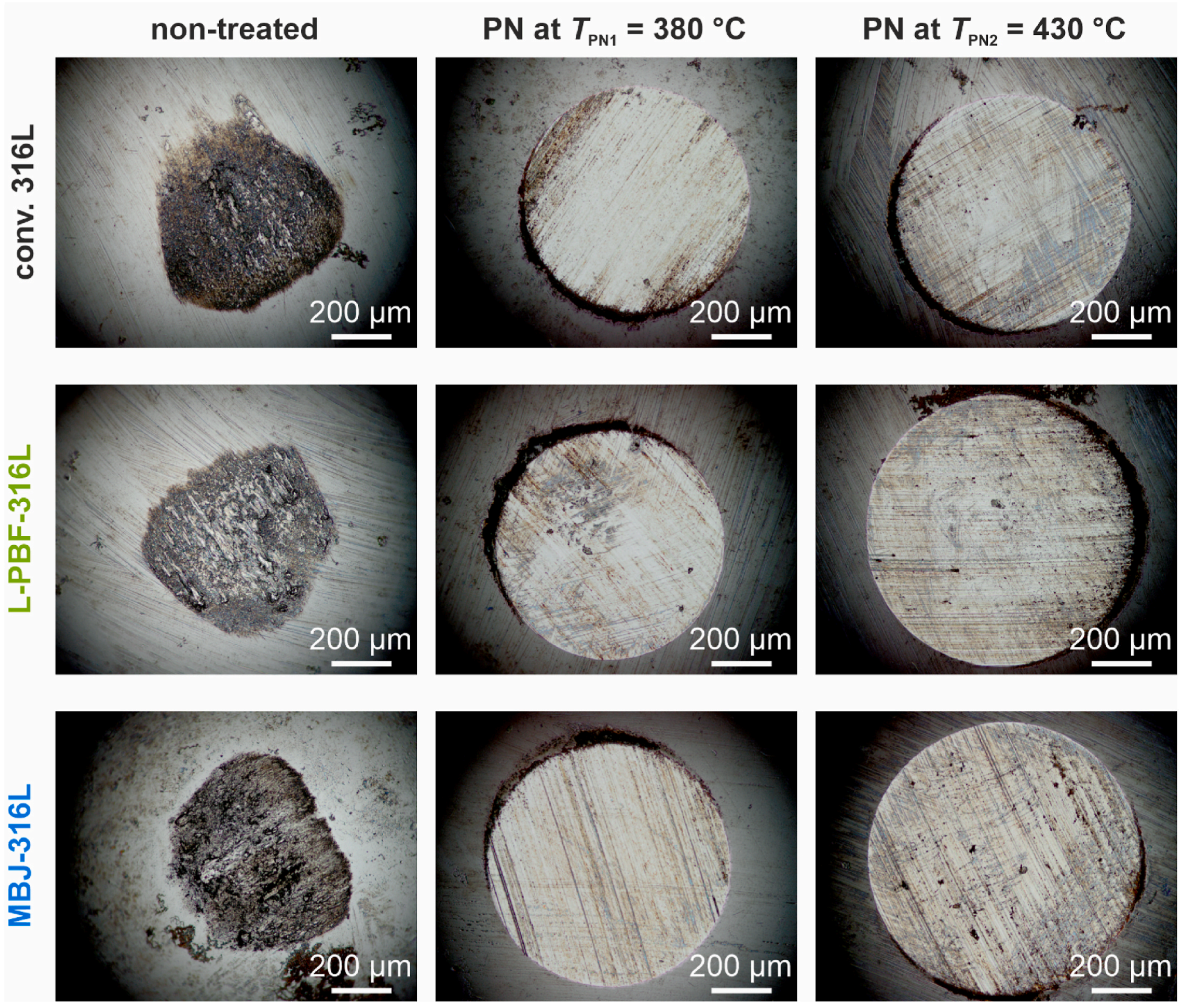

Fig. 9. Light micrographs of the worn AISI 52100 ball counterparts tested against the conventionally manufactured (conv.) 316L, L-PBF 316L, and MBJ 316L in non-treated and plasma nitrided conditions.

$(8 \pm 1) \times 10^{-5}$ mm^3/Nm, while MBJ-316L shows the highest wear rate of $k \approx (57 \pm 3) \times 10^{-5}$ mm^3/Nm. The 3D profiles of non-treated 316L reveal plastic displacement of material to the sides along the wear tracks, while SEM images show disrupted and smeared material along the wear track. The pronounced abrasive and plastic wear is primarily attributed to the low hardness of non-treated 316L. Accordingly, the wear resistance of the non-treated steels correlates with hardness, as low hardness values lead to reduced abrasive wear resistance. The worn material of 316L in the non-nitrided condition smears on the AISI 52100 ball counterpart and forms a material transfer, as shown by the light micrographs of the ball counterparts.

For all differently manufactured steels, higher friction is observed in the plasma nitrided condition. The highest COF values ranging from 0.78 to 0.84 are obtained by 316L plasma nitrided at the highest temperature $T_{PN2} = 430$ °C. The increase in friction is attributed to both higher roughness and increased hardness. Harder roughness asperities enhance the deformative friction component in the contact zone. All plasma nitrided 316L steels do not exhibit abrasive wear, which is attributed to the higher near-surface hardness of the S phase layer compared to the AISI 52100 counterpart. However, material transfer from the softer AISI 52100 steel is observed along the wear track, as evidenced by the 3D surface profiles and SEM micrographs. In this regard, the extent of material transfer is lower for 316L steels plasma nitrided at $T_{PN2} = 430$ °C compared to those treated at $T_{PN2} = 380$ °C, suggesting that higher surface roughness reduces the smearing of the softer AISI 52100 counterpart. In this regard, the AISI 52100 counterpart experiences increased abrasive wear against the plasma nitrided 316L steels. The highest wear rates ranging from 1.4×10^{-5} mm^3/Nm to 2.4×10^{-5} mm^3/Nm are observed for plasma nitrided 316L at $T_{PN2} = 430$ °C. This effect is attributed to the increased hardness and roughness of the nitrided surface, as the roughness asperities exert an abrasive effect on the softer ball. This is clearly visible in the light micrographs of the AISI 52100 balls, where a segment of the ball has been removed in the frictional contact, and furrows have formed on the contact surface. It can be concluded that plasma nitriding leads to similar friction and wear behavior across the differently manufactured 316L steels.

For tribological applications of additively manufactured 316L steels, it is essential not only to enhance the wear resistance of the base material but also to minimize overall friction and wear on the counterpart. Under non-lubricated friction conditions, friction-reducing amorphous carbon coatings can be employed for this purpose. Previous studies by the authors have demonstrated that amorphous carbon coatings applied on additively manufactured 316L and AISI 630 (17-4 PH) steels exhibit high adhesion, comparable to that of conventionally manufactured steels, and significantly reduce friction and wear [24,48]. However, the low hardness of the substrate material promotes increased plastic deformation of the substrate/coating system under high mechanical loads. Plasma nitriding improves the mechanical load-bearing capacity of the substrate, thereby enhancing the overall mechanical and tribological performance of additively manufactured steels when combined with an additional coating in a duplex treatment. In this context, the

thickness of the S phase layer should be tailored to the specific loading conditions of the application to ensure sufficient Vickers microhardness in the substrate for withstanding the applied mechanical loads.

4. Conclusions

Additively manufactured 316L steels produced by L-PBF and MBJ were plasma nitrided by advanced AEGD technology at $T_{PN1} = 380$ °C and $T_{PN2} = 430$ °C for 10 h and compared to conventionally wrought 316L. The following main conclusions can be drawn.

- While L-PBF exhibits characteristic melt pool boundaries and MBJ shows larger sintered grains, the manufacturing route does not significantly alter the formation of the S phase.
- The thickness of the S phase is primarily temperature-dependent, reaching values of $\delta_{PN1} \approx 3$ µm at T_{PN1} and $\delta_{PN2} \approx 12$ µm at T_{PN2}. The consistency of these thicknesses across all manufacturing variants is attributed to similar lattice parameters and, consequently, comparable diffusion rates of nitrogen within austenite grains.
- Surface roughness increases following etching and further during plasma nitriding. The highest *Ra* and *Rz* values are obtained at T_{PN2} due to greater volumetric expansion.
- Plasma nitriding significantly increases surface hardness, with nanoindentation values of 1230–1400 HV_{IT} at T_{PN1} and 1420–1520 HV_{IT} at T_{PN2}. However, Vickers microhardness is limited by the core properties, with MBJ steel variants showing lower overall values than L-PBF due to their initial microstructure.
- In dry sliding tests against 52100 steel, plasma nitriding increases friction because of the higher surface roughness but significantly improves the resistance against abrasive wear, with only material transfer from the softer counterpart observed.

Overall, plasma nitriding of additively manufactured 316L achieves mechanical and tribological performance comparable to plasma nitrided wrought 316L. This confirms a high degree of process transferability, demonstrating that established industrial plasma nitriding processes can be reliably applied to L-PBF and MBJ components to achieve predictable layer properties. While the core microstructure influences the load-bearing capacity, the surface properties of the expanded austenite phase remain consistent across all manufacturing variants.

CRediT authorship contribution statement

Nelson Filipe Lopes Dias: Conceptualization, Data curation, Formal analysis, Investigation, Project administration, Visualization, Writing – original draft. Julia Urbanczyk: Writing – review & editing. Dominic Stangier: Conceptualization, Writing – review & editing. Patrick Köhnen: Resources, Writing – review & editing. Christopher Schaak: Resources, Writing – review & editing. Simon Höges: Resources, Writing – review & editing. Wolfgang Tillmann: Resources, Supervision, Writing – review & editing.

Declaration of competing interest

The authors declare that they have no known competing financial interests or personal relationships that could have appeared to influence the work reported in this paper.

Acknowledgments

The authors gratefully acknowledge the financial support of the Deutsche Forschungsgemeinschaft (DFG, German Research Foundation, Germany) within the project 348145475 (TI 343/130-3). The authors also extend their gratitude Mr. Tim Schäfer and Mr. Ingo Schäper from the Institute of Materials Engineering (TU Dortmund University) for conducting the metallographic preparation and white light microscopic investigations. Furthermore, the authors thank Prof. Dr.-Ing. Dirk Biermann and Dr. Alexander Meijer from the Institute of Machining Technology (TU Dortmund University) for providing the confocal 3D microscope.

Appendix A. Supplementary data

Supplementary data to this article can be found online at https://doi.org/10.1016/j.jmrt.2026.02.042.

References

[1] Bajaj P, Hariharan A, Kini A, Kürnsteiner P, Raabe D, Jägle EA. Steels in additive manufacturing: a review of their microstructure and properties. Materials Science and Engineering: A 2020;772:138633. https://doi.org/10.1016/j.msea.2019.138633.
[2] Fayazfar H, Salarian M, Rogalsky A, Sarker D, Russo P, Paserin V, Toyserkani E. A critical review of powder-based additive manufacturing of ferrous alloys: process parameters, microstructure and mechanical properties. Mater Des 2018;144:98–128. https://doi.org/10.1016/j.matdes.2018.02.018.
[3] Yadroitsev I, Yadroitsava I, Du Plessis A. Basics of laser powder bed fusion. In: Yadroitsev I, Yadroitsava I, Du Plessis A, MacDonald E, editors. Fundamentals of laser powder bed fusion of metals. Amsterdam, Kidlington, Oxford, Cambridge, MA: Elsevier; 2021. p. 15–38.
[4] Narasimharaju SR, Zeng W, See TL, Zhu Z, Scott P, Jiang X, Lou S. A comprehensive review on laser powder bed fusion of steels: processing, microstructure, defects and control methods, mechanical properties, current challenges and future trends. J Manuf Process 2022;75:375–414. https://doi.org/10.1016/j.jmapro.2021.12.033.
[5] Mostafaei A, Elliott AM, Barnes JE, Li F, Tan W, Cramer CL, Nandwana P, Chmielus M. Binder jet 3D printing – process parameters, materials, properties, and challenges. Prog Mater Sci 2020:100707. https://doi.org/10.1016/j.pmatsci.2020.100707.
[6] Ziaee M, Crane NB. Binder jetting: a review of process, materials, and methods. Addit Manuf 2019;28:781–801. https://doi.org/10.1016/j.addma.2019.05.031.
[7] Zitelli Folgarait, Schino Di. Laser powder bed fusion of stainless steel grades: a review. Metals 2019;9:731. https://doi.org/10.3390/met9070731.
[8] Mirzababaei S, Pasebani S. A review on binder jet additive manufacturing of 316L stainless steel. 2019.
[9] Marshall P. Austenitic stainless steels: microstructure and mechanical properties. London usw: Elsevier Applied Science Publ; 1984.
[10] Yang WJ, Zhang M, Zhao YH, Shen ML, Lei H, Xu L, Xiao JQ, Gong J, Yu BH, Sun C. Enhancement of mechanical property and corrosion resistance of 316L stainless steels by low temperature arc plasma nitriding. Surf Coating Technol 2016;298:64–72. https://doi.org/10.1016/j.surfcoat.2016.04.045.
[11] Li G, Peng Q, Li C, Wang Y, Gao J, Chen S, Wang J, Shen B. Effect of DC plasma nitriding temperature on microstructure and dry-sliding wear properties of 316L stainless steel. Surf Coating Technol 2008;202:2749–54. https://doi.org/10.1016/j.surfcoat.2007.10.002.
[12] Fossati A, Borgioli F, Galvanetto E, Bacci T. Corrosion resistance properties of glow-discharge nitrided AISI 316L austenitic stainless steel in NaCl solutions. Corros Sci 2006;48:1513–27. https://doi.org/10.1016/j.corsci.2005.06.006.
[13] Jeong B-Y, Kim M-H. Effects of pulse frequency and temperature on the nitride layer and surface characteristics of plasma nitrided stainless steel. Surf Coating Technol 2001;137:249–54. https://doi.org/10.1016/S0257-8972(00)01095-1.
[14] Lei MK, Zhu XM. Plasma-based low-energy ion implantation of austenitic stainless steel for improvement in wear and corrosion resistance. Surf Coating Technol 2005;193:22–8. https://doi.org/10.1016/j.surfcoat.2004.08.139.
[15] de Las Heras E, Ybarra G, Lamas D, Cabo A, Dalibon EL, Brühl SP. Plasma nitriding of 316L stainless steel in two different N2-H2 atmospheres - influence on microstructure and corrosion resistance. Surf Coating Technol 2017;313:47–54. https://doi.org/10.1016/j.surfcoat.2017.01.037.
[16] Mingolo N, Tschiptschin AP, Pinedo CE. On the formation of expanded austenite during plasma nitriding of an AISI 316L austenitic stainless steel. Surf Coating Technol 2006;201:4215–8. https://doi.org/10.1016/j.surfcoat.2006.08.060.
[17] Gokcekaya O, Ergun C, Gulmez T, Nakano T, Yilmaz S. Structural characterization of ion nitrided 316L austenitic stainless steel: influence of treatment temperature and time. Metals 2022;12:306. https://doi.org/10.3390/met12020306.
[18] Xu XL, Wang L, Yu ZW, Hei ZK. Microstructural characterization of plasma nitrided austenitic stainless steel. Surf Coating Technol 2000;132:270–4. https://doi.org/10.1016/S0257-8972(00)00905-1.
[19] Samandi M, Shedden BA, Smith DI, Collins GA, Hutchings R, Tendys J. Microstructure, corrosion and tribological behaviour of plasma immersion ion-implanted austenitic stainless steel. Surf Coating Technol 1993;59:261–6. https://doi.org/10.1016/0257-8972(93)90094-5.
[20] Godec M, Donik Č, Kocijan A, Podgornik B, Skobir Balantič DA. Effect of post-treated low-temperature plasma nitriding on the wear and corrosion resistance of 316L stainless steel manufactured by laser powder-bed fusion. Addit Manuf 2020;32:101000. https://doi.org/10.1016/j.addma.2019.101000.
[21] Lin K, Qiao J, Gu D, Wang H, Shi B, Zhang W, Shan J, Xu Y, Tian L. Active screen plasma nitriding of laser powder bed fusion processed 316L stainless steel for the

application of fuel cell bipolar plates. Virtual Phys Prototyp 2023;18:e2225490. https://doi.org/10.1080/17452759.2023.2225490.
[22] Kumar V, Pruncu CI, Wang Y, Figueroa CA, Singh I, Hosmani SS. The role of microstructure modifications on electrochemical and plasma-nitriding behaviour of 316L steel produced by laser powder bed fusion. Philos Mag 2023;103:1855–96. https://doi.org/10.1080/14786435.2023.2241019.
[23] Yazıcı M, Çomaklı O, Yetim T, Yetim AF, Çelik A. Investigation of mechanical, tribological and magnetic properties after plasma nitriding of AISI 316L stainless steel produced with different orientations angles by selective laser melting. Surf Coating Technol 2023;467:129676. https://doi.org/10.1016/j.surfcoat.2023.129676.
[24] Tillmann W, Lopes Dias NF, Stangier D, Schaak C, Höges S. Coatability of diamond-like carbon on 316L stainless steel printed by binder jetting. Addit Manuf 2021;44:102064. https://doi.org/10.1016/j.addma.2021.102064.
[25] Stangier D, Lopes Dias NF, Henning T, Ontrup F, Tillmann W, von der Heide V. Improved plasma etching and nitriding technology for enhanced PVD coating performance using advanced arc enhanced glow discharge. Surf Coating Technol 2025;497:131753. https://doi.org/10.1016/j.surfcoat.2025.131753.
[26] Lopes Dias NF, Meijer AL, Jäckel CP, Frisch A, Biermann D, Tillmann W. Arc-enhanced glow discharge ion etching of WC-Co cemented carbide for improved PVD thin film adhesion and asymmetric cutting edge preparation of micro milling tools. Surf Coating Technol 2024;491:131166. https://doi.org/10.1016/j.surfcoat.2024.131166.
[27] Dimitrov VI, D'Haen J, Knuyt G, Quaeyhaegens C, Stals LM. A method for determination of the effective diffusion coefficient and sputtering rate during plasma diffusion treatment. Surf Coating Technol 1998;99:234–41. https://doi.org/10.1016/S0257-8972(97)00530-6.
[28] German Institute for Standardization DIN. Geometrical product specifications (GPS) - surface texture: profile - part 3: specification operators (ISO 21920-3:2021); German version EN ISO 21920-3:2022. 2022.
[29] Eigenmann B, Macherauch E. Röntgenographische Untersuchung von Spannungszuständen in Werkstoffen. In: Teil III. Fortsetzung von Matwiss. und Werkstofftechn. Heft 3/1995, S. 148–160 und Heft 4/1995, S. 199–216, vol. 27. Materialwissenschaft Werkst; 1996. p. 426–37. https://doi.org/10.1002/mawe.19960270907.
[30] Waseda Y, Matsubara E, Shinoda K. Diffraction from polycrystalline samples and determination of crystal structure. In: Waseda Y, Matsubara E, Shinoda K, editors. X-Ray diffraction crystallography. Berlin, Heidelberg: Springer Berlin Heidelberg; 2011. p. 107–67.
[31] Borgioli F. From austenitic stainless steel to expanded Austenite-S phase: formation, characteristics and properties of an elusive metastable phase. Metals 2020;10:187. https://doi.org/10.3390/met10020187.
[32] Borgioli F. The "expanded" phases in the low-temperature treated stainless steels: a review. Metals 2022;12:331. https://doi.org/10.3390/met12020331.
[33] Öztürk O, Williamson DL. Phase and composition depth distribution analyses of low energy, high flux N implanted stainless steel. J Appl Phys 1995;77:3839–50. https://doi.org/10.1063/1.358561.
[34] Mändl S, Günzel R, Richter E, Möller W, Rauschenbach B. Annealing behaviour of nitrogen implanted stainless steel. Surf Coating Technol 2000;128–129:423–8. https://doi.org/10.1016/S0257-8972(00)00645-9.
[35] Marchev K, Landis M, Vallerio R, Cooper C, Giessen B. The m phase layer on ion nitrided austenitic stainless steel (III): an epitaxial relationship between the m phase and the γ parent phase and a review of structural identifications of this phase. Surf Coating Technol 1999;116–119:184–8. https://doi.org/10.1016/S0257-8972(99)00296-0.
[36] Bacci T, Borgioli F, Galvanetto E, Pradelli G. Glow-discharge nitriding of sintered stainless steels. Surf Coating Technol 2001;139:251–6. https://doi.org/10.1016/S0257-8972(01)01010-6.
[37] Marchev K, Cooper CV, Blucher JT, Giessen BC. Conditions for the formation of a martensitic single-phase compound layer in ion-nitrided 316L austenitic stainless steel. Surf Coating Technol 1998;99:225–8. https://doi.org/10.1016/S0257-8972(97)00532-X.
[38] Fewell MP, Priest JM. High-order diffractometry of expanded austenite using synchrotron radiation. Surf Coating Technol 2008;202:1802–15. https://doi.org/10.1016/j.surfcoat.2007.07.062.
[39] Plaut RL, Herrera C, Escriba DM, Rios PR, Padilha AF. A short review on wrought austenitic stainless steels at high temperatures: processing, microstructure, properties and performance. Math Res 2007;10:453–60. https://doi.org/10.1590/S1516-14392007000400021.
[40] Manova D, Mändl S, Neumann H, Rauschenbach B. Formation of metastable diffusion layers in Cr-containing iron, cobalt and nickel alloys after nitrogen insertion. Surf Coating Technol 2017;312:81–90. https://doi.org/10.1016/j.surfcoat.2016.09.059.
[41] Vetter J, Wallendorf T. Plasma diagnostics of arc-enhanced glow discharge. Surf Coating Technol 1995;76–77:322–7. https://doi.org/10.1016/0257-8972(95)02554-5.
[42] Rauschenbach B. Low-energy ion irradiation of materials. Cham: Springer International Publishing; 2022.
[43] Liang W, Xiaolei X, Jiujun X, Yaqin S. Characteristics of low pressure plasma arc source ion nitrided layer on austenitic stainless steel at low temperature. Thin Solid Films 2001;391:11–6. https://doi.org/10.1016/S0040-6090(01)00969-5.
[44] Asgari M, Barnoush A, Johnsen R, Hoel R. Microstructural characterization of pulsed plasma nitrided 316L stainless steel. Materials Science and Engineering: A 2011;529:425–34. https://doi.org/10.1016/j.msea.2011.09.055.
[45] Öztürk O, Okur S, Riviere JP. Structural and magnetic characterization of plasma ion nitrided layer on 316L stainless steel alloy. Nucl Instrum Methods Phys Res Sect B Beam Interact Mater Atoms 2009;267:1540–5. https://doi.org/10.1016/j.nimb.2009.01.076.
[46] Agrawal AK, Singh A. Limitations on the hardness increase in 316L stainless steel under dynamic plastic deformation. Materials Science and Engineering: A 2017;687:306–12. https://doi.org/10.1016/j.msea.2017.01.066.
[47] Xu M, Guo H, Wang Y, Hou Y, Dong Z, Zhang L. Mechanical properties and microstructural characteristics of 316L stainless steel fabricated by laser powder bed fusion and binder jetting. J Mater Res Technol 2023;24:4427–39. https://doi.org/10.1016/j.jmrt.2023.04.069.
[48] Tillmann W, Lopes Dias NF, Stangier D, Schaak C, Höges S. Heat treatment of binder jet printed 17–4 PH stainless steel for subsequent deposition of tribo-functional diamond-like carbon coatings. Mater Des 2022;213:110304. https://doi.org/10.1016/j.matdes.2021.110304.